Quantifying the heterogeneity of the tectonic stress field using borehole data

Martin Schoenball[1,2*] and Nicholas C. Davatzes[1]

[1] Earth and Environmental Science, Temple University, Philadelphia, Pennsylvania, USA

[2] GMEG Science Center, U.S. Geological Survey, Menlo Park, California, USA

*now at Stanford University, Department of Geophysics, Stanford, California, USA

Major points:
-   Local and global borehole data show that heterogeneity of stress is a site characteristic
-   Stress characterization requires suitably long logs to quantify orientation and heterogeneity
-   Deviated boreholes can be reliably analyzed for stress orientations

Abstract

The heterogeneity of the tectonic stress field is a fundamental property which influences earthquake dynamics and subsurface engineering. Self-similar scaling of stress heterogeneities is frequently assumed to explain characteristics of earthquakes such as the magnitude-frequency relation. However, observational evidence for such scaling of the stress field heterogeneity is scarce.

We analyze the local stress orientations using image logs of two closely spaced boreholes in the Coso Geothermal Field with sub-vertical and deviated trajectories, respectively, each spanning about 2 km in depth. Both the mean and the standard deviation of stress orientation indicators (borehole breakouts, drilling-induced fractures and petal-centerline fractures) determined from each borehole agree to the limit of the resolution of our method although measurements at specific depths may not. We find that the standard deviation in these boreholes strongly depends on the interval length analyzed, generally increasing up to a wellbore log length of about 600 m and constant for longer intervals. We find the same behavior in global data from the World Stress Map. This suggests that the standard deviation of stress indicators characterizes the heterogeneity of the tectonic stress field rather than the quality of the stress measurement. A large standard deviation of a stress measurement might be an expression of strong crustal heterogeneity rather than of an unreliable stress determination. Robust characterization of stress heterogeneity requires logs that sample stress indicators along a representative sample volume of at least 1 km.

1 Introduction

Heterogeneity of stress in the Earth's crust is an elusive quantity which impacts earthquake dynamics [*Mai and Beroza*, 2002; *Ampuero et al.*, 2006; *Hsu et al.*, 2010], behavior of aftershock sequences [*Hardebeck*, 2010; *Smith and Dieterich*, 2010], and reservoir engineering and operation [*Cornet et al.*, 2007]. The state of stress and pore fluid pressure is a crucial property that defines which faults are prone to slip and which ones are stable [*Morris et al.*, 1996]. It is assumed that the heterogeneities of the stress field such as stress rotations and stress concentrations due to e.g. contrasting rheology [*Wileveau et al.*, 2007], elastic parameters or active faults [*Shamir and Zoback*, 1992; *Barton and Zoback*, 1994; *Yale*, 2003] play a crucial role in many subsurface processes. Commonly, self-similar stress fields are assumed to explain geophysical phenomena including the magnitude-frequency relation of earthquakes [*Andrews*, 1980; *Huang and Turcotte*, 1988]. While direct observations of self-similarity of the stress field are rare [*Shamir and Zoback*, 1992; *Day-Lewis et al.*, 2010], the self-similar stress field model is supported by other observations of self-similar scaling of geologic phenomena related to the stress field. For example, geometric fault roughness has been found to be self-similar from length scales of micrometers to kilometers [*Candela et al.*, 2012] and the size and frequency distribution of natural fractures follows self-similar scaling [*Barton and Zoback*, 1992; *Ben-Zion*, 2008].

Regional and global data sets show that tectonic stress varies smoothly and continuously, revealing coherent domains of stress [*Müller et al.*, 1992; *Zoback*, 1992; *Heidbach et al.*, 2010, *Reiter et al.*, 2014]. Whether the motion of tectonic plates determines the principal orientation of stress or if secondary phenomena are required to explain the observed variation of the tectonic stress field is still debated [*Heidbach et al.*, 2007; *Heidbach et al.*, 2016]. Resolving stress variations on a scale of core to boreholes often shows strong heterogeneities [*Shamir and Zoback*, 1992; *Barton and Zoback*, 1994; *Sahara et al.*, 2014] that are sometimes described using fractal scaling laws [*Day-Lewis et al.*, 2010]. Often, the observed variation over several meters is larger than the variation of derived mean stress orientations

on a regional scale. Rivera and Kanamori [2002] discuss the two endmembers for the crustal stress field of (1) a smooth stress field and variable friction or (2) a constant friction and variable stress field. They conclude that both models are mutually exclusive and in the most likely case both friction and the stress tensor exhibit considerable variation. Motivated by these endmember viewpoints there is ongoing discussion of whether the stress field is smooth and the observed heterogeneity apparent from earthquake moment tensors are due to measurement uncertainties or whether the stress field is dominated by fractal scaling of heterogeneity [*Hardebeck*, 2006, 2010, 2015; *Smith and Dieterich*, 2010; *Smith and Heaton*, 2011, 2015].

Data in support of the smooth stress and heterogeneous stress hypotheses mostly come from earthquake focal mechanisms and boreholes, respectively. Hardebeck [2010] argues that stress is measured at large depth for earthquakes and shallow depth for boreholes. Differences in depth are accompanied by differences in rock rheology resulting in smoothing of stress at greater depth and retention of stress heterogeneities at shallow depth [*Pierdominici and Heidbach*, 2012]. Furthermore, we have to note the different length scales that are sampled by these different data sets. Borehole logging and especially the retrieval of acoustic or electric borehole images provides detailed insights on the subsurface stress conditions at the meter scale [*Barton and Moos*, 2010; *Davatzes and Hickman*, 2010] spanning intervals of up to several kilometers. With a sampling rate of about 5 mm even sub-millimeter wide fractures can be reliably detected due to the high resistivity contrasts of fluid-saturated fractures embedded in dense country rock. Similarly, roughness due to fractures intersecting the boreholes wall reveal similarly sized fractures in acoustic logs. Thus, image logs covering well trajectories for several kilometers can be used to study stress indicators such as borehole breakouts and drilling-induced fractures on length scales spanning about four orders of magnitude in the first 5 or so kilometers of the Earth's crust.

Heterogeneity of stress in boreholes has been widely observed to correlate with natural fractures and faults [e.g. *Bell et al.*, 1992; *Shamir and Zoback*, 1992; *Barton and Zoback*, 1994; *Mariucci et al.*, 2002; *Yale*, 2003, *Pierdominici et al.*, 2011; *Sahara et al.*, 2014; *McNamara et al.*, 2015; *Rajabi et al.*, 2015] and lithology changes [*Wileveau et al.*, 2007]. A self-similar scaling of stress heterogeneity observed in boreholes has been first proposed by Shamir and Zoback [1992], and Day-Lewis et al. [2010] aim to link this to the magnitude-frequency distribution of earthquakes. However, as has been shown by Valley and Evans [2014], the uncertainties in determining the scaling coefficient from discontinuous records of stress orientation can be significant and the actual link between observed heterogeneity of stress and scaling of earthquake magnitudes remains to be confirmed. Furthermore, we point out here the discrepancy between the competing concepts of self-similar scaling of stress heterogeneity [*Shamir and Zoback*, 1992; *Day-Lewis et al.*, 2010] and the mechanistic description of interaction of natural fractures that leads to discontinuities of stress in the country rock [*Barton and Zoback*, 1994; *Valley et al.*, 2014].

Evidence for characteristic length scales, i.e. a breakdown of the self-similar scaling, has been presented for major fault zones in Southern California by Bailey et al. [2010]. Using focal mechanism data, they show that different fault zones exhibit different degrees of heterogeneity of derived focal mechanisms. They link the observed differences to variations of cumulative displacement, a measure of fault maturity.

In this paper we aim to close the gap between descriptions of stress heterogeneity from single boreholes and fault zone earthquake data. We analyze the local stress orientations in two closely spaced

boreholes drilled from the same well pad. We find evidence for a characteristic length scale of the stress heterogeneity. Then, we compare our findings with global data from the World Stress Map (WSM) project [*Heidbach et al.*, 2016]. The paper is organized as follows: In Section 2 we describe the tectonic setting in the study area before we introduce our methodology to analyze stress indicators in boreholes with significant deviation in Section 3. In Section 4 we apply this approach to the two boreholes to retrieve a characterization of the stress field for each borehole. We compare their results with emphasis on the overall mean orientation of horizontal stress and its local heterogeneity. In Section 5 we analyze the heterogeneity of stress along the borehole trajectory and in relation to global WSM data. We establish that the degree of stress heterogeneity is scale-dependent up to a characteristic length scale of about 1 km and the amplitude of stress heterogeneity is a site characteristic.

2   Geologic setting and well data

In the first part of this paper, we analyze stress indicators on image logs spanning a total of 4.5 km along the trajectories of the two wells 58-10 and 58A-10 (wellheads at 35.999°N, 117.740°W) situated just east of the Coso Geothermal Field in the Eastern California Shear Zone. The Coso area lies in the releasing step between the Owens Valley fault to the north and the Airport Lake fault to the south, as suggested by Unruh et al. [2002] and Monastero et al. [2005]. As such, the area is subjected to strike-slip motion and Basin and Range-style extension (Figure 1). This is evidenced by Holocene normal fault scarps [*Unruh and Streig*, 2004], geodetic velocities of up to 30 mm/a of extension [*Wicks et al.*, 2001] and 6.5 mm/a dextral shear [*McClusky et al.*, 2001]. Faults of which we know the sense of motion are normal faults [*Jayko*, 2009]. The two wells are located in the Coso Wash area. This is a sedimentary basin between the exploited Coso Geothermal Field to the west that is bounded on the east side by the Coso Wash fault, and the series of normal faults of the Wild Horse Mesa to the east (Figure 1). The Coso Wash is filled with about 600 m of sediments overlaying igneous basement rocks (predominantly diorite, granodiorite and quartz diorite) and interrupted by volcanic intrusions. The two wells have been drilled from the same well pad with a sub-vertical and a build-and-hold trajectory, respectively, leading to lateral separations of 20 to 300 m between the wells. In order to facilitate reading, hereafter we annotate the sub-vertical (v) well 58A-10^v and the deviated (d) well 58-10^d. They were drilled in 1997 and 2000, respectively, to potentially extend the producing field to the east. However, both wells were found to be uneconomical and were not put in production. At the writing of this manuscript, the immediate vicinity (distances < 1 km) has not shown significant levels of seismicity (relative to the very active Coso East Flank area at distances > 1 km further west) and we assume that the wells sampled a natural stress state, unperturbed by the production operations in the geothermal field at the time of logging [*Schoenball et al.,* 2015].
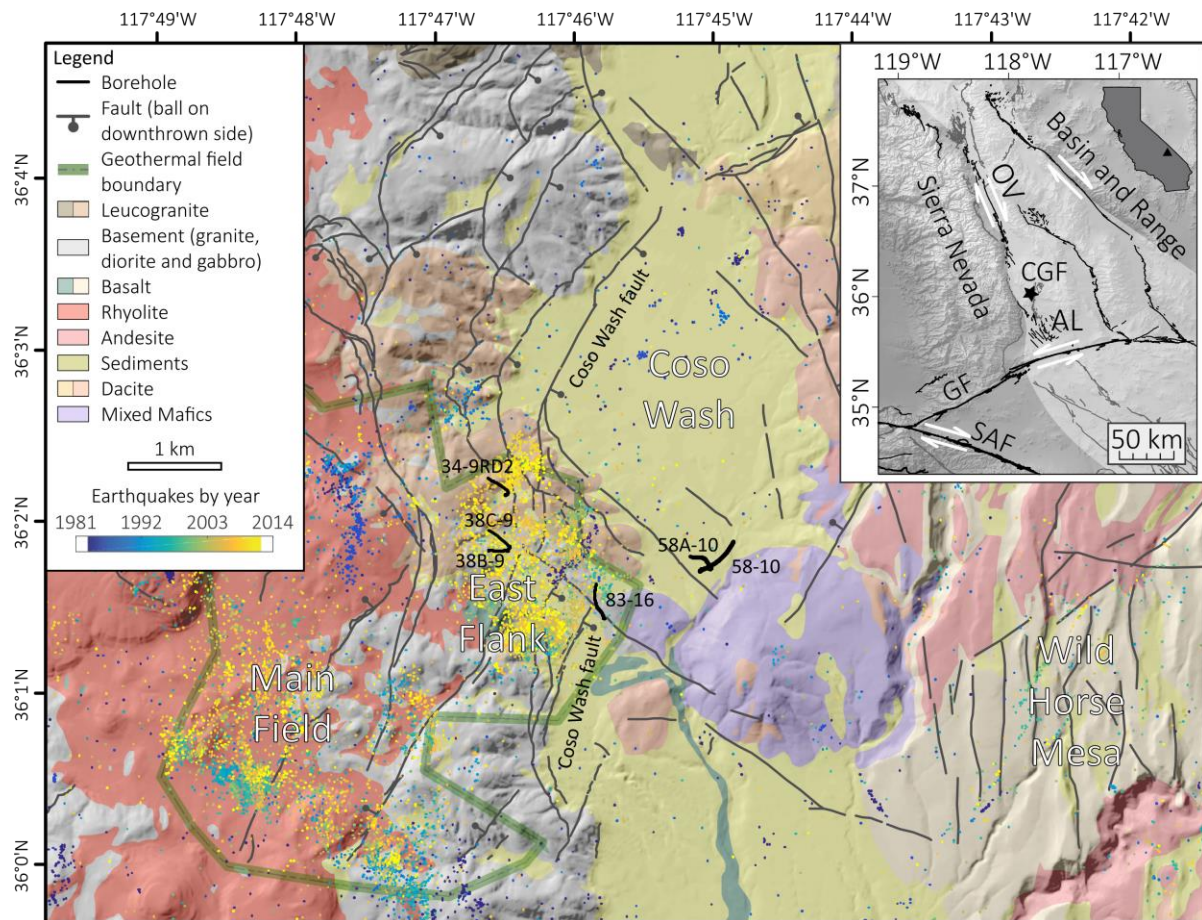
Figure 1: Geological map of the Coso Geothermal Field (CGF) area with projections of the borehole trajectories to the surface of boreholes 58-10^d and 58A-10^v and other wells mentioned in the text. Earthquakes (colored dots) are from Hauksson et al., [2012]. Faults are from Jayko [2009]. The inset shows the tectonic setting of the CGF in the Eastern California Shear Zone to Walker Lane complex (bright shading). GF = Garlock Fault, SAF = San Andreas Fault, OV = Owens Valley Fault, AL = Airport Lake Fault. The upper right corner shows the location of the map in the state of California.
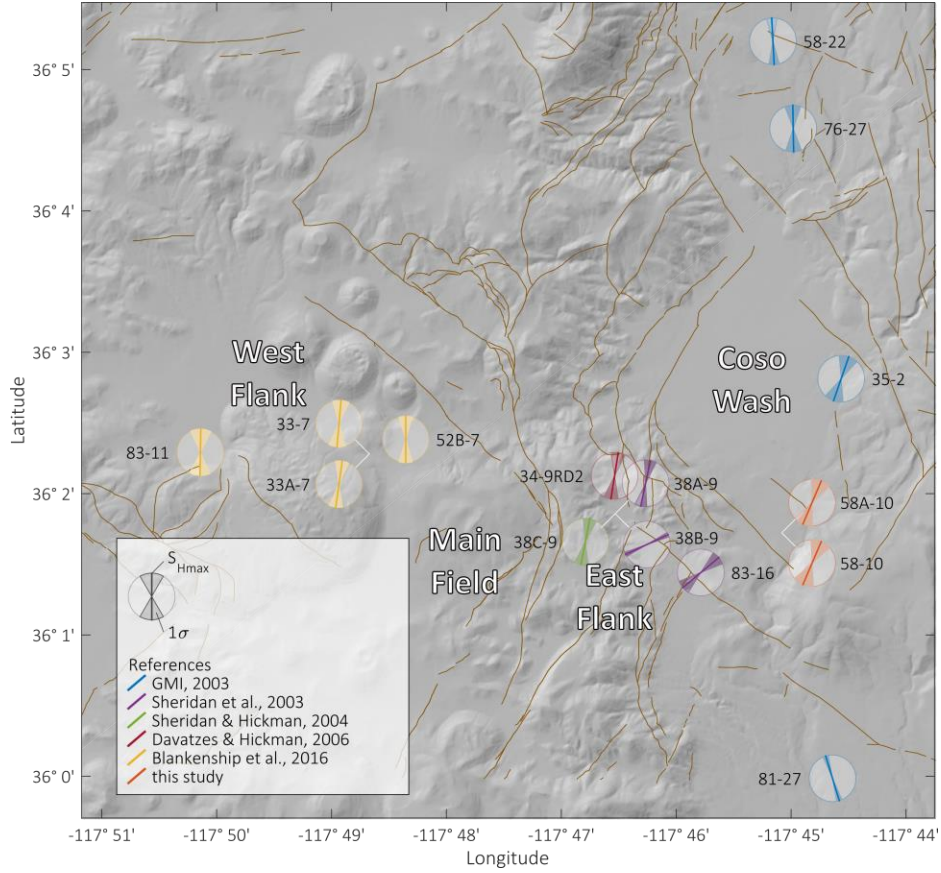
Figure 2: Compilation of stress determinations in and around the Coso Geothermal Field. Rose diagrams are centered on the well heads unless several symbols would overlap in which case white lines point to the well heads.

The stress field at Coso has been studied extensively, from boreholes, from earthquake data [*Feng and Lees*, 1998; *Unruh et al.*, 2002], and using numerical modelling [*Eckert and Connolly*, 2007]. Based on stress indicators interpreted from image logs of the Coso East Flank and the Coso Wash areas, a roughly north-south orientation ±20° of the maximum horizontal stress S_{Hmax} has been determined [*Sheridan et al.*, 2003; *Sheridan and Hickman*, 2004; *Davatzes and Hickman*, 2006, 2010]. Generally, large heterogeneity in this stress azimuth was encountered along each well, with standard deviations of the individual stress indicators on the order of ±25° from the local mean orientation (Figure 2). In some intervals, an apparent rotation of the stress field by 90° has been observed [*Davatzes and Hickman*, 2006] and the orientation of S_{Hmax} obtained from wells 38B-9 and 83-16 are outliers with S_{Hmax} oriented at N65°E ±6° and N50°E ±18°, respectively [*Sheridan et al.*, 2003]. While the reported standard deviations are relatively small, the coverage by stress indicators is sparse in these wells.

Using two hydrofrac tests performed in well 38C-9 (East Flank of the Coso Geothermal Field), Sheridan and Hickman [2004] obtained S_{hmin} = 0.63 S_v assuming a rock density of 2630 kg/m³ obtained from a density log. Another hydrofrac test performed in well 34-9RD2 confirms the low value for S_{hmin} [*Davatzes and Hickman*, 2006]. They measure S_{hmin} = 38.85 MPa at 2383 m depth, which corresponds to S_{hmin} = 0.62 S_v. To estimate the magnitude of the maximum horizontal stress, rock strength parameters were acquired from laboratory experiments [*TerraTek*, 2004; *Morrow and Lockner*, 2006]. Based on these, and the absence of borehole breakouts, Davatzes and Hickman [2006] infer S_{Hmax} to be in the range 1.2 S_v < S_{Hmax} < 1.9 S_v if the region is in strike-slip faulting. Since we do observe borehole breakouts (see

below), we know that S_{Hmax} should be towards the higher end of this range. Normal faulting was observed in Holocene sediments along the Coso Wash fault scarps, consistent with low frictional strength of clay minerals such as illite [*Morrow et al.*, 1992]. Hence, the area is in a transitional state between normal and strike-slip faulting, consistent with focal mechanisms of local earthquakes [*Yang et al.*, 2012].

Well 58-10^d was drilled sub-vertically to about 1200 m and then deviated by up to 42° towards the NNE direction (Figure 3). Well 58A-10^v was drilled from the same well pad in a sub-vertical trajectory to 3100 m measured depth. It was further deepened in 2003 but we do not have data that covers this later stage of the well. The deviation of 58A-10^v in the logged interval does not exceed 12° (Figure 3). Both wells were logged with Schlumberger's Formation MicroImager (FMI) tool in the upper 8.5-inch sections and with the Formation MicroScanner (FMS) tool in the lower 6.125-inch sections [*Davatzes and Hickman*, 2010]. Additionally, well 58A-10^v was logged with an acoustic borehole televiewer-type ALT ABI85 tool in the deeper 6.125-inch section [*Davatzes and Hickman*, 2010].

The electric tools (FMI and FMS) rely on an array of buttons distributed on pads that are attached to the tool and pressed on the borehole wall by spring-loaded arms. These tools image only a fraction of the borehole wall (about 50% in our case), which depends on the well diameter and the size of the tool's pads. The acoustic tool uses an ultrasonic focused pulse that scans the entire borehole wall; it provides images of the amplitude and travel time. The travel time image can be used to reconstruct the cross-sectional shape of the borehole and is ideal for borehole breakout interpretation. The electrical and acoustic tools image contrasts in resistivity and acoustic impedance, respectively. Because of that, they can detect features that are far smaller than the nominal pixel size of about 5 mm. Both tools are capable of detecting cracks as thin as about 0.1 mm [*Davatzes and Hickman*, 2010]. Therefore, these logs are extremely sensitive to small cracks and even bedding or foliation. For a detailed description and comparison of acoustic and electric tools employed in well 58A-10^v we refer to the thorough discussion by Davatzes and Hickman [2010] and references therein.
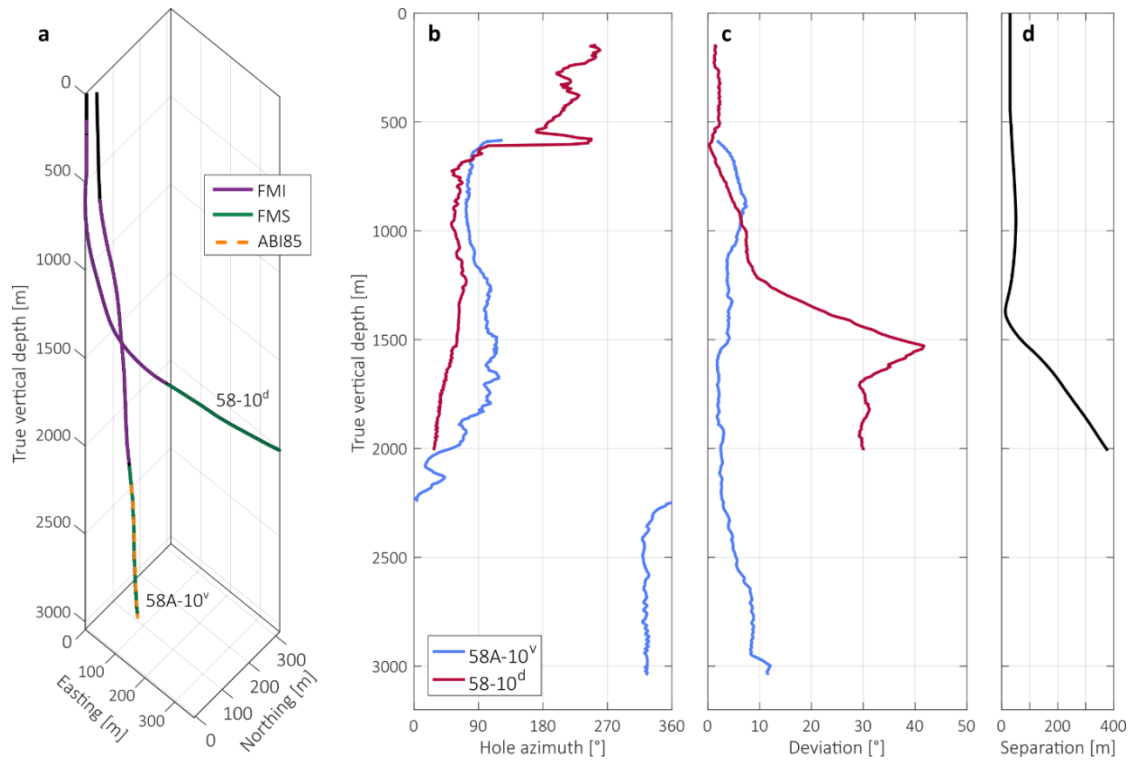
Figure 3: Well trajectories of wells 58A-10^v and 58-10^d. (a) 3-D view with colors referring to the available image logging data. (b) Hole azimuth clockwise from north, (c) borehole deviation from vertical and (d) the lateral separation of the two boreholes, all along true vertical depth.

3   Methods

The elastic solutions for the stress field around a cylindrical opening [*Kirsch*, 1898] predict compressive stress along the circumference of boreholes to be largest at azimuths aligned with the minimum stress, leading to the formation of borehole breakouts (BO). These were first observed and used for analysis of the orientation of the stress field in the Earth's crust by Bell and Gough [1979]. Similarly, tensile stress is observed along the borehole wall at azimuths aligned with the maximum compressive stress, leading to drilling-induced tensile failure (DIF) of the borehole wall (Figure 4). Today, the analysis of breakouts and drilling-induced tensile fractures in vertical wells is a standard procedure in well log analysis [e.g. *Zoback et al.*, 2003; *Schmitt et al.*, 2012]. The common approach implicitly assumes that the borehole axis coincides with one principal stress. In practice, the vertical stress component S_v is assumed to coincide with one principal stress component. If the well is inclined with respect to the principal axes of the stress field, the axis of borehole failure no longer coincides with the borehole axis. Instead, the location of BOs and DIFs along the borehole wall is dependent on the magnitudes of the principal stresses and the orientation of the borehole relative to the principal stress axes. Thus, interpretation of the orientation of horizontal stresses becomes non-unique and dependent on the principal stress magnitudes as well as their directions relative to the borehole trajectory. The effect of borehole inclination is small and can be neglected for wells that do not deviate more than about 12° from the vertical [*Mastin*, 1988]. Beyond that, the relation describing the location of BOs and DIFs becomes non-linear and sensitive to the relative magnitudes of the principal stresses.
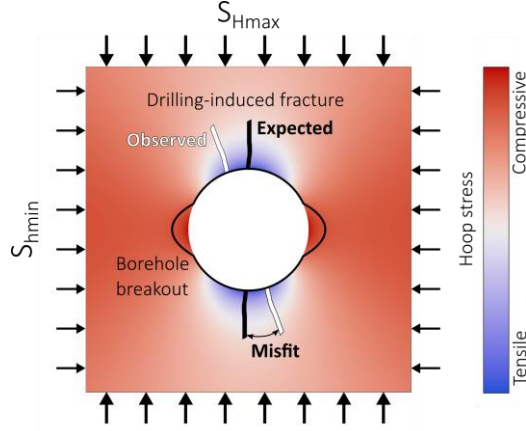
Figure 4: Hoop stress around a circular well in an infinite plate with relative compressive sections along S_{hmin}, leading to breakouts; and relative tensile sections along S_{Hmax}, leading to Drilling-induced fractures (DIF). Hypothetical observed DIFs are sketched in white with the misfit angle between the expected and observed locations of DIFs.

The forward problem for borehole failure in inclined wells was solved by Hiramatsu and Oka [1962] and various complex inversion schemes for the non-linear inverse problem have been developed [*Aadnoy*, 1990a; *Qian and Pedersen*, 1991; *Zajac and Stock*, 1997; *Thorsen*, 2011]. Since deviated boreholes typically sample the stress tensor at a variety of relative orientations, the onset and relative position of borehole failure as a function of deviation could potentially provide constraints on stress magnitudes. The underlying assumption of such an approach is that the remote orientations and ratios among the principal stresses are constant throughout the sampled volume [*Wiprut et al.*, 1997]. Similarly, information from several nearby inclined wells can be combined to constrain stress magnitudes, assuming that all wells considered are subjected to the same stress field [*Aadnoy*, 1990a]. Inversion schemes find the best-fitting stress tensor, but generally the resolution for general stress states is poor due to noise introduced by heterogeneity of the rock mass. It is difficult to assess the robustness of stress states inferred from these schemes. Subsequently, we use a grid search based on the solutions of the forward model to gain better insight on the relative misfit of stress states to the borehole data.

3.1 Stress in inclined boreholes

Stresses around a borehole oriented orthogonally to principal stresses were derived by Kirsch [1898] for plane strain conditions. In this manuscript, we use the rock mechanics sign convention with positive stresses for compression. At the borehole wall, the Terzhagi effective stresses σ in a cylindrical coordinate system are:

$$\sigma_{\theta\theta} = S_{hmin} + S_{Hmax} - 2(S_{Hmax} - S_{hmin}) \cos 2\theta - p_0 - p_w$$

$$\sigma_{rr} = p_w - p_0 \tag{1}$$

$$\sigma_{zz} = S_v - 2\nu(S_{Hmax} - S_{hmin}) \cos 2\theta - p_0$$

with the maximum and minimum total horizontal stresses S_{Hmax} and S_{hmin}, respectively, the vertical stress S_v, Poisson's ratio ν and p_w the borehole mud pressure acting on the borehole wall and p_0 is the pore pressure in the formation. The angle θ is measured clockwise from the orientation of S_{Hmax}. The hoop stress $\sigma_{\theta\theta}$ reaches a maximum along S_{hmin}, leading to the formation of breakouts if a failure criterion for compressive failure is met. The minimum of $\sigma_{\theta\theta}$ is reached in the direction of S_{Hmax} and tensile cracks may form at the borehole wall if the tensile strength of the rock is overcome. The

solutions for a more general case, valid for boreholes inclined with respect to the stress tensor, have first been derived by Hiramatsu and Oka [1962]. We briefly outline here the necessary transformations to obtain stresses in the rotated borehole coordinate system but refer to Peška and Zoback [1995] and Zoback [2010] for the full treatment of the problem.

In the general case, the borehole axis is not parallel to a principal stress and the principal stresses acting on the borehole wall prescribe an angle with the borehole axis. They are obtained from transforming the stresses in a geographical coordinate system to a coordinate system along the borehole wall. To obtain the stress tensor S_b in the coordinate system parallel to the borehole axis the first step is to obtain the stress components S_g in a geographic coordinate system from the principal components of the stress tensor S_s [Peška and Zoback, 1995] using a tensor rotation:

$$S_b = R_b R_s^T S_s R_s R_b^T \tag{2}$$

Here, R_s is the rotation matrix from the coordinate system defined by the principal stresses to the geographic coordinate system. R_b is the rotation matrix from the geographic coordinate system to the borehole coordinate system with the reference frame defined by the borehole axis and high side of the borehole [Peška and Zoback, 1995]. Then, the effective principal stresses acting on the borehole wall are given by

$$\sigma_{tmax} = \frac{1}{2}\left(\sigma_{zz} + \sigma_{\theta\theta} + \sqrt{(\sigma_{zz} - \sigma_{\theta\theta})^2 + 4\tau_{\theta z}^2} \right)$$

$$\sigma_{tmin} = \frac{1}{2}\left(\sigma_{zz} + \sigma_{\theta\theta} - \sqrt{(\sigma_{zz} - \sigma_{\theta\theta})^2 + 4\tau_{\theta z}^2} \right) \tag{3}$$

$$\sigma_{rr} = \Delta p$$

where $\sigma_{zz}, \sigma_{\theta\theta}$ and $\tau_{\theta z}$ are the effective stresses in the cylindrical coordinate system of S_b along an arbitrarily oriented borehole (Figure 5). Borehole breakouts occur where σ_{tmax} is above the compressive strength of the rock formation and tensile failure occurring where σ_{tmin} is below the tensile strength of the rock. The magnitudes of σ_{tmax} and σ_{tmin} vary along the circumference of the borehole as $\sigma_{\theta\theta}$ varies with azimuth, depending on the trajectory of the borehole in the geographical coordinate system. The locations of the extrema of σ_{tmax} and σ_{tmin} are dependent on the relative magnitudes of the principal stresses and may vary strongly among stress regimes if the borehole deviation is larger than about 12° [Mastin, 1988]. The dependence of the location of extrema of the hoop stress on the relative stress magnitudes is non-linear. Specifically, the locations of stress indicators in a geographic reference frame are not directly related to the orientation of the stress tensor. For the subsequent analysis, we reference stress indicators to the high side of the well (i.e. the highest point along a circumference) as opposed to north, which is usually used as reference for the analysis of vertical wells.
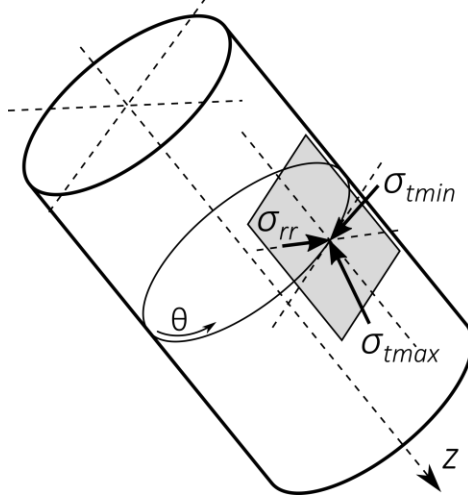
Figure 5: Principal stresses σ_{tmax}, σ_{tmin}, and σ_{rr} at the wall of an inclined borehole. σ_{tmax} and σ_{tmin} act tangentially to the borehole wall, while σ_{rr} acts perpendicular to the borehole wall. (after *Peška and Zoback*, 1995).

It is interesting to note that for a given stress field there are well trajectories (given by azimuth and deviation) for which the relative angle between the expected locations of BOs and DIFs is significantly different from 90°. In the vicinity of these trajectories plotted in a lower hemisphere projection, stress indicators significantly change their location along the borehole circumference for only marginal changes of the well trajectory. A detailed discussion of this phenomenon is given in Zajac and Stock [1997]. For strike-slip stress states these nodal points lie at the outer edge of the lower hemisphere projection, i.e. they are relevant for wells inclined to a horizontal trajectory. For the wells discussed in this paper, this phenomenon is not relevant.

3.2 Grid search for best-fitting stress state

Assuming that compressive failure in the Earth's crust is described by the Mohr-Coulomb criterion and tensile failure occurs when the pore fluid pressure is above the least principal stress, and that the vertical stress S_v is a principal stress [*Anderson*, 1951], all equilibrium stress states are bounded by a polygon given by [*Jaeger and Cook*, 1979, *Zoback et al.*, 2003]:

$$S_{hmin} \geq \frac{S_v - p_0}{\left(\sqrt{\mu^2 + 1} + \mu\right)^2} + p_0$$

$$S_{Hmax} \leq \left(\sqrt{\mu^2 + 1} + \mu\right)^2 (S_v - p_0) + p_0 \tag{4}$$

$$S_{Hmax} \leq \left(\sqrt{\mu^2 + 1} + \mu\right)^2 (S_h - p_0) + p_0$$

and $S_{Hmax} \geq S_{hmin}$ with the coefficient of friction μ; cohesion is assumed negligible. The Andersonian stress regimes as part of the polygon of stress states are then defined by triangles with normal faulting for $S_v \geq S_{Hmax} \geq S_{hmin}$, strike-slip faulting for $S_{Hmax} \geq S_v \geq S_{hmin}$ and thrust faulting for $S_{Hmax} \geq S_{hmin} \geq S_v$. Note that we assume S_v to be one principal stress component. This is the same assumption that is implicitly made during the common interpretation of vertical wells.

In the grid search, we sample all stress states that fall within the stress polygon on a regular grid. We chose a high value of 1 for μ to account for all possible stress states. Values higher than that are typically not observed [*Lockner and Beeler*, 2002]. Similarly, for pore pressure p_0 we assume a low value of 0.37 S_v, corresponding to a fluid density of 1000 kg/m³ with the water table at the surface and an overburden density of 2700 kg/m³. All stress states are normalized by the vertical stress magnitude S_v which defines the natural scale for stress magnitudes that we use throughout this paper. With that, we assume constant stress gradients for all principal stresses and pore pressure along the vertical. This assumption might not be permitted in areas with strata that act as a fluid barrier or show pronounced ductile behavior. For example, inter-bedding of argillaceous formations that exhibits a pronounced rheological contrast evidenced by differential creep and stress relaxation can lead to variable stress gradients [*Wileveau et al.*, 2007]. Hydraulic compartments created by cap rock layers may create over- and under-pressured zones frequently encountered in hydrocarbon systems. However, in the crystalline rock formation that we deal with here a stress decoupling that leads to variable stress gradients is not expected. Anomalous pore pressure gradients are not observed in the Coso Geothermal Field [*Davatzes and Hickman*, 2006].

For our analysis we need to infer the expected location along the borehole wall of the maximum and minimum of σ_{tmax} and σ_{tmin}, respectively. For each observed borehole feature *k*, we compute the angular difference $m_k(i,j)$ between the observed location and the expected location of that feature according to equation (3) for all stress states *i* outlined by the stress polygon and for all orientations of S_{Hmax} *j* between N0°E and N179°E. For each assumed stress state *(i, j)* we then sum the absolute misfits m_k for all stress indicators (Equation 5).

$$m(i,j) = \sum_k m_k(i,j)l_k \tag{5}$$

To account for the different lengths of stress indicators, we weighted the individual misfit of each indicator according to its length l_k. The best-fitting stress state *(i,j)* is then given by the absolute minimum of *m(i,j)*. As discussed below, the stress indicators show a strong scatter about a mean orientation. Furthermore, there are sections that show a strongly different orientation of stress indicators than in the majority of the well. The L1-norm was chosen for the misfit over other norms since it does not over-emphasize such outliers in the data. Since the variation of *m(i,j)* over different stress magnitude states tends to be small compared to its absolute value, we do not focus on finding the single best-fitting set of stress gradient magnitudes but interpret our results for a range of stress magnitude states.

3.3 Stress indicators and image logs

To analyze the stress field from borehole images, stress indicators need to be identified and located (these structures are extensively reviewed by *Zoback et al.*, 2003; *Schmitt et al.*, 2012). These indicators consist of either tensile or compressive failure of the borehole wall induced by the concentration of stress at the free surface of the borehole, which symmetrically distributed about the borehole circumference (Figure 4). Both wells show an abundance of drilling-induced (tensile) fractures along most sections of the well. In well 58A-10ᵛ a number of compressive borehole breakouts were identified. For DIFs and BOs we pick both sides individually, which may be separated azimuthally by 180±20° due to interaction with natural fractures and other heterogeneities such as material contrasts in the rock mass. Additionally, we interpret petal-centerline fractures in well 58A-10ᵛ. These tensile fractures are induced

by excessive weight on the drill bit and are commonly observed in core [*Li and Schmitt*, 1998; *Zhang*, 2011; *Schmitt et al.*, 2012]. In some cases, such as in well 58A-10^v, they propagate far enough to penetrate the borehole wall and can be imaged in subsequent logging runs [*Davatzes and Hickman*, 2010]. The petal part of petal-centerline fractures forms along the orientation of S_{hmin} and the centerlines converge towards DIFs along S_{Hmax}. Typically, the separation of the centerlines is different from 180°. We pick both sides of the centerline and compute the average as a measurement of the S_{hmin} direction. Figure 6 shows examples of interpreted stress indicators for the electrical and acoustic log in borehole 58A-10^v. For further details of the interpretation of these logs and stress indicators we refer to the thorough discussion in Davatzes and Hickman [2010]. The picked stress indicators along the trajectory of each well are shown in Figures S1 and S2.

To interpret the stress tensor responsible for the borehole wall failure, the acquired image needs to be oriented in a reference frame and then features located (picked) on the image. Both steps are prone to errors. In order to estimate the uncertainties of locating stress indicators we used the deep section of 58A-10^v where both the FMS and ABI85 logs were acquired. We picked characteristic features in both logs and compare their determined azimuth. With that method, we estimate the repeatability of this analysis (orientation of the tool in the well) convoluted with the picking error involved in manual interpretation of such images. We obtain a good agreement between both images and the differential azimuths of picked features follows a normal distribution with a standard deviation of 4.3° (Figure S3). The normal distribution centered about 0° indicates the randomness of the measurements and an absence of systematic errors in the processing of both log types.
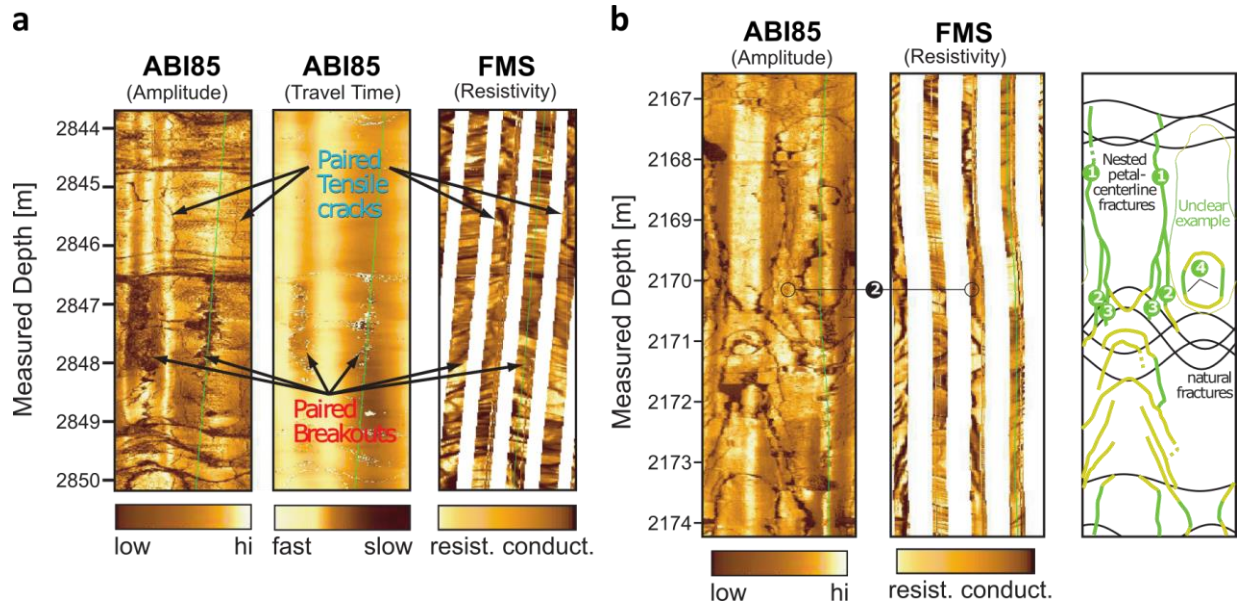

Figure 6: Examples of stress indicators in image logs of borehole 58A-10^v. (a) Drilling-induced fractures were imaged equally well in both logs. Breakouts are well imaged by the ABI85 log but are mostly unidentifiable on the FMS, but their position is indicated for comparison. (b) Nested petal-centerline fractures are imaged in both log types. Related centerline fractures are indicated as numbered pairs, which are commonly connected by petals that are evident in the BHTV image but not in the FMS image. Note that at approximately 2170 m measured depth both petal and centerline fractures intersect with and sometimes abut against preexisting natural fractures. Modified from Davatzes and Hickman [2010].

4 Results

We present the results of our grid search as maps of (1) the minimal misfit for the sampled stress states for any stress orientation (Figures 7a, b) and of (2) the orientation of S_{Hmax} for which that minimal misfit is obtained (Figures 7c, d). To obtain the best-fitting stress state, we have to find stress states that give a reasonably small misfit in the minimal misfit maps (Figures 7a, b) and then refer to the maps of best-fitting stress orientation (Figures 7c, d) to obtain the orientation of S_{Hmax}. The inset in Figure 7a shows the behavior of the misfit for one given stress magnitude state while varying the assumed orientation of S_{Hmax}.

Being a near vertical well, 58A-10^v does not show any preference for a particular stress state and consequently the minimal misfit is almost constant along all Andersonian stress states (Figure 7a). This is an expected result, since vertical wells cannot be used to distinguish between stress regimes from the position of BOs and DIFs alone. The variation that we obtain is due to the limited effect of the well deviation (up to 12°), that is fully accounted for in our analysis. The best-fitting S_{Hmax} orientation varies only minimally between N21°E and N23°E for most normal faulting and all strike-slip stress states and down to 13° for degenerate ($S_{Hmax} \approx S_{hmin}$) normal faulting and thrust faulting stress states (Figure 7c). For stress magnitudes we use the preferred stress magnitude state from Davatzes and Hickman [2006]. Since we do observe breakouts in 58A-10^v, we conclude that the magnitude of S_{Hmax} is towards the higher end of the range provided. Using $S_{Hmax} = 1.8\ S_v$ and $S_{hmin} = 0.65\ S_v$ we obtain a best-fitting orientation of S_{Hmax} at N23°E.

Well 58-10^d has a considerable number of stress indicators in both its near-vertical and strongly deviated sections. It therefore samples the stress tensor in different directions – along the vertical direction in the shallow section and along a NNW trajectory deviated by about 30° in the deeper section. This added information further constrains the stress state. The minimal misfit map strongly rejects a thrust faulting regime and favors all strike-slip stress states and normal faulting stress states with S_{Hmax} close to S_v (Figure 7b). While the lowest misfit is found for strike-slip faulting stress states with $S_{hmin} \approx S_v$, the differences of the derived misfit values to that for other strike-slip stress states are on the same order or less than the error of picking stress indicators (see above) and we do not consider them meaningful.

In Figure 8 we plot the difference of Figures 7c-d to compare the preferred stress orientations in both wells. The inferred stress orientations for stress states preferred by well 58-10^d agree with that inferred from well 58A-10^v (Figure 7c-d). The variation in best-fitting stress orientations between the two wells for the preferred stress states is within 5°. For the rejected stress states this difference can be much larger, but there is no physical meaning to this. Assuming the preferred stress magnitude state as above, we obtain a best-fitting orientation of S_{Hmax} at N22°E.

In our analysis above, we have determined the best-fitting stress orientation for the entire sampled sections of each well. Here, both wells yield basically the same stress orientation and the difference of 1° lies entirely within the uncertainty of the picking of stress indicators and correctly orienting the image logs. To assess the quality of a stress measurement, the standard deviation (SD) of individual stress indicators weighted by their length is typically used [*Heidbach et al.*, 2010]. For inclined wells we assume the preferred stress state and compute the local misfit between the expected and observed location of each stress indicator. SD is then computed from these misfit values and weighted by feature length. Here, both limbs of BOs and DIFs are measured individually while a pair of petal-centerline fractures

yields only one measurement. In Figure 9 we show the rose diagrams of stress indicators that were computed based on the resolved best-fitting stress state and the misfit for each stress indicator.

The difference in the mean stress orientations of the two wells is substantially smaller than their observed SD despite their differences in deviation. In addition, we also obtain nearly the same SD of 22.6° for 58A-10^v and 23.8° for 58-10^d. In conclusion, the same remote stress orientation and gradients in the magnitude of principal stresses fit the entire depth interval sampled by both wells. In addition, the variability of the local stress measurements quantified through SD is similarly consistent.
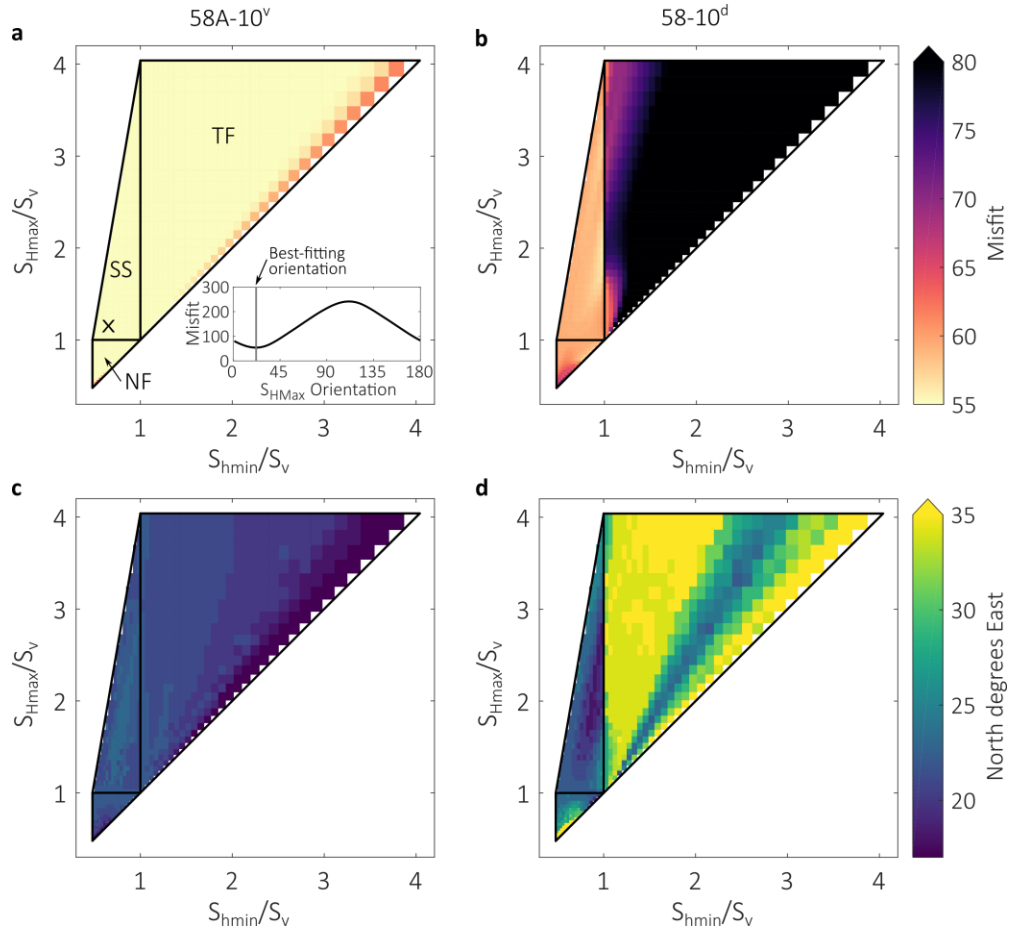

Figure 7: Maps of (a, b) Minimum angular misfit (arbitrary units) for all stress indicators along sampled Andersonian stress states and any stress orientation. NF, SS and TF labels correspond to the Andersonian stress regimes that each triangle represents. The inset in (a) shows the misfit as a function of the assumed orientation of S_{Hmax} for the stress magnitude state indicated by the x. The values plotted are the minimal misfit values for each stress magnitude state. (c, d) show the best-fitting orientation of S_{Hmax} (the x-value of the minimum in the inset in (a)) along all Andersonian stress states for wells 58-10^d and 58A-10^v, respectively. Pointy ends of color bars indicate clipped color maps used for better visualization.
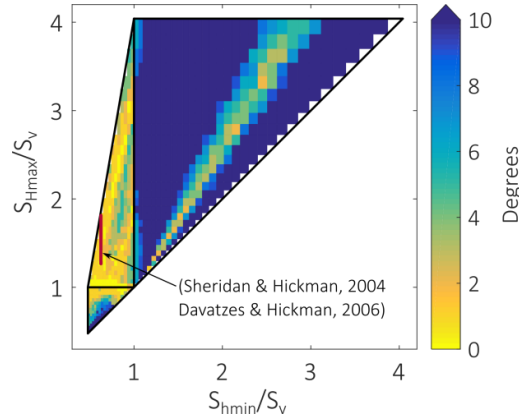
Figure 8: Angular misfit between best-fitting stress orientations for wells 58-10^d and 58A-10^v and Andersonian stress states as shown in Figure 7(c,d). The stress state derived by Sheridan and Hickman [2004] and Davatzes and Hickman [2006] is marked. Note that the color map is clipped at 10°.
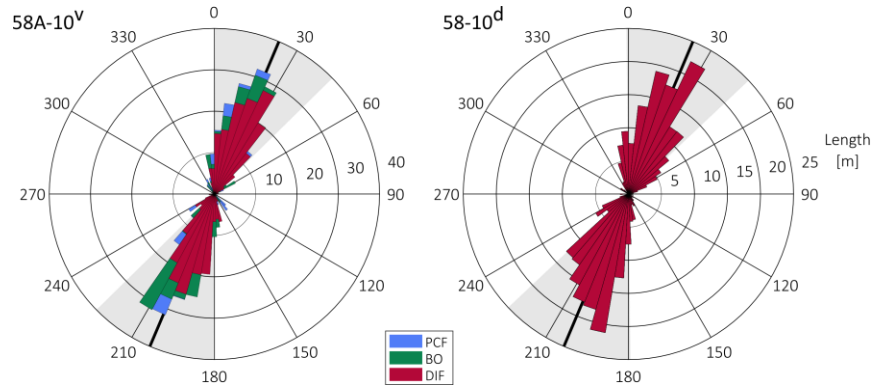

Figure 9: Rose diagram of stress indicators in wells 58A-10^v and 58-10^d transformed to a geographic coordinate system as they would occur in vertical wells. The light shaded area marks one standard deviation to both sides of the best-fitting mean stress orientation.

4.1 Local stress orientation

By assuming that each stress indicator samples the local state of stress on the meter scale, we can analyze the local stress orientation. In Figure 10a-b we show the local misfit of individual stress indicators relative to the best-fitting orientation of S_{Hmax} for each entire well. To compare the local stress orientations obtained for both wells, we apply a median filter to the misfit values for smoothing. The median preserves discontinuities of the local stress state as they are expected near faults and other geologic structures [e.g., *Shamir and Zoback*, 1992]. Furthermore, these deviations are conserved by the median filter over intervals where the density of picked features varies. Since we have discontinuous data, we could either apply the filter over a constant number of samples or over a constant length interval. For the case of constant sample number, we obtain the median stress orientation at a sample by taking the median of local stress orientations between 10 samples above and 10 samples below the target sample for a total of 21 samples. For the case of constant window length, we take the median of all samples within 20 m above and 20 m below the target depth resulting in a 40 m window length (Figure 10a-c).
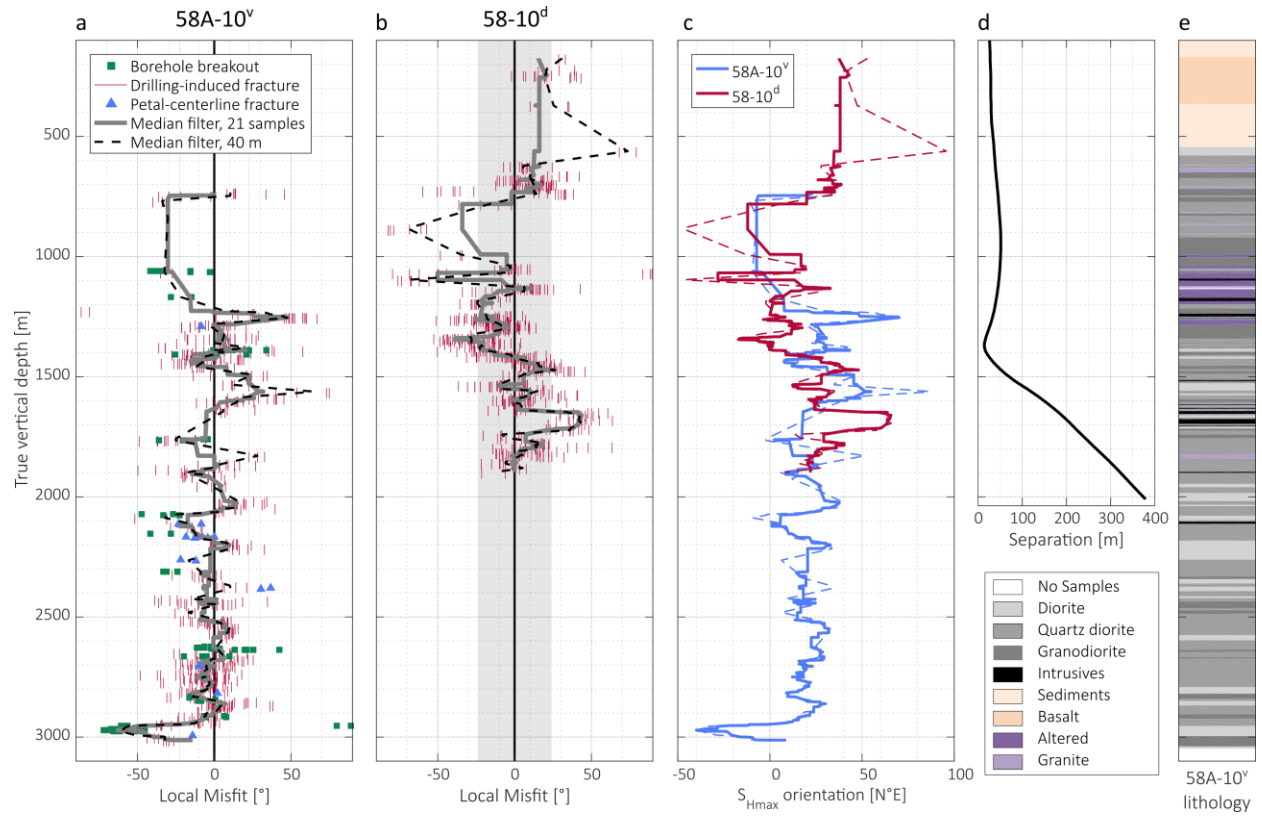
Figure 10: Stress indicators and derived local misfit relative to the best-fitting orientation of S_{Hmax} for (a) well 58A-10^v and (b) well 58-10^d. Figure (c) is a comparison of median-filtered local stress orientation for both wells and (d) shows the horizontal separation between the wells and (e) is shows a simplified lithology column from the 58A-10^v mud log. All plots are along the same true vertical depth axis.

The stress state in both wells is well sampled along more than 2 km and by more than 700 individual stress indicators for each well. This dense sampling reveals as strong variation of the local stress orientation around the tectonic mean stress orientation. We observe continuous variations of the local stress orientation with typical amplitudes of the deviations of around 20° and wavelengths from 50 to 500 m. The unfiltered data shows variations of the local stress orientation of similar amplitude at the scale of meters and abrupt, discontinuous rotations near faults and fractures. Importantly, the deviation of the local stress state along the trajectories does not show any trend with depth (Figure 10a-b). This is evidence that we have resolved the true mean orientation of the tectonic part of the stress tensor.

Apart from the seemingly random scatter of individual stress indicators, we observe a number of systematic rotations of the local stress state, consistently sampled over several 10s of stress indicators and spanning up to more than 100 m along depth. The almost continuous sampling by DIFs in the deeper half of the logged 58-10^d well clearly shows a smooth transition in stress orientations between 1350 and 1500 m over more than 60° in azimuth (Figure 10b). Further down this well, a discontinuous rotation of S_{Hmax} by about 40° is observed at about 1640 m. Although there are a number of fractures visible on the image logs in this interval, no major fault zone could be clearly associated with this transition in the local stress orientation. We also note frequent changes of lithology in this depth section that may be responsible for the observed rotation (see below).

In the deepest interval of 58A-10^v (2900-3050 m), we observe a change of the failure pattern from DIFs to BOs that goes along with a rotation of the horizontal stress orientation by 60° (Figure 10a). This rotation coincides with a lithology change from quartz diorite to diorite and to granodiorite below. Of all the crystalline rock units occurring in the field, diorite is known to have the lowest rock strength. Morrow and Lockner [2006] find a uniaxial compressive strength of 186 MPa for diorite and 277 MPa for granodiorite samples collected in well 34-9RD2, 2 km to the west. Additionally, they find that diorite is stiffer than the tested granodiorite (Young's moduli of 100 GPa and 75 GPa, respectively) and has a higher Poisson's ration (0.27 and 0.31, respectively) leading to stress concentrations in diorite section and potentially to stress rotations due to the contrasting elastic and frictional parameters. Therefore, the stiffer but weaker diorite sections are much more likely to show BO formation than those through granodiorite.

Comparing the local stress orientations in both wells at a given depth (Figure 10c) we do not observe a 1:1 agreement. Instead, we observe differences in the local stress orientation at corresponding depth that are consistent with the overall variability along both wells. We observe the closest agreement of the local stress orientation in the section where both wells are the closest (around 1370 m). It is interesting to note that the local stress orientation follows undulations of similar wavelength and amplitude in the section from 1270-1530 m in 58-10^d and about 70 m deeper in 58A-10^v. We do not have sufficient knowledge of the 3-D structure near the wells to explain this behavior. However, it is plausible that a large-scale system of faults and igneous intrusions provides the mechanical conditions needed for such a parallel variation.

4.2 Coso stress map

In Figure 2, we show a compilation of stress determinations performed previously in an around the Coso Geothermal Field together with our results. We may notice a trend of the resolved orientation of S_{Hmax} from slightly east of north in the Coso Wash area to S_{Hmax} oriented due north in the Coso West Flank area, that was analyzed by Blankenship et al., 2016. We notice the stress measurements in wells 38B-9, 81-27 and 83-16, that appear to be inconsistent with the other measurements. Furthermore, the former two wells have very low reported SD, indicative of a "trustworthy" stress measurement.

However, in well 81-27 only a handful of DIFs, spanning a depth range of about 130m were identified [*GMI*, 2013]. The situation is similar with the analysis of well 38B-9 in a 370m long interval. Additionally, the FMS logging tool used in this well provides only partial azimuthal coverage compounded by the fact that the tool did not rotate during the logging run. Overall, the borehole wall could not be imaged representatively and we are doubtful about this determination of the stress orientation. In the following section we will analyze what influence the logging interval has on resolving the orientation of S_{Hmax} and the measured SD.

5 Discussion

In the approach presented above we use the location of axial tensile failure and borehole breakouts to infer the best-fitting stress state for inclined well trajectories. A feature we did not integrate in our analysis are en-echelon DIFs [*Peška and Zoback*, 1995; *Barton and Moos*, 2010; *Thorsen*, 2011]. In that case the angle between the DIF and the borehole axis provides further information on the orientation of the stress tensor relative to the borehole axis [*Aadnoy*, 1990b]. In clear image logs of more homogeneous media, such as sediments, these features can provide direct evidence for stress states at an angle with the borehole axis. In our case, most of the borehole failure occurs in highly fractured

crystalline rock where propagation of drilling-induced fractures is strongly perturbed. The presence of natural fractures can lead to ambiguity that prevents accurate picking, leading us to neglect some observations where the interpretation of natural fracture versus induced fracture is ambiguous. Consequently, we did not observe consistent en-echelon DIFs even in the strongly deviated sections of borehole 58-10[d]. Here, the deviation of DIFs with respect to the well axis is expected to be about 16° if the vertical is indeed a principal stress orientation.

In this study, we treat the observed azimuthal variation of stress indicators as direct evidence for heterogeneities of the local stress field. This stance is based on the assumption of validity of the Kirsch solutions (Equations 1), and of frictional equilibrium governing failure, e.g. described by the Mohr-Coulomb criterion. We have quantified the error of orienting and interpreting image logs with a standard deviation of 4.3° (Figure S3). Another new assumption is a constant pore pressure gradient. Indeed, for the Coso region pore pressure was observed to be in hydrostatic equilibrium [*Davatzes and Hickman*, 2006]. Below we discuss possible sources of the observed stress heterogeneity.

5.1 Sources of stress heterogeneity

There has been extensive investigation into the sources of stress heterogeneity observed in boreholes and it is beyond the scope of this paper to discuss them in detail. However, below we review some of the previous work to establish that our observations of stress heterogeneity for two wells in the Coso region are not spurious. Instead, our observations represent significant heterogeneity of stress, which has been observed in many boreholes, both in sedimentary and crystalline rocks.

Small-scale heterogeneity appears to be dominated by the interaction of borehole failure and existing natural fractures [*Bobet and Einstein*, 1998; *Healy et al.*, 2006]. Induced fractures tend to coalesce with pre-existing natural fractures to minimize fracture surface energy. Abutting relationships between induced features and natural fractures are frequently observed [*Davatzes and Hickman*, 2010; *Sahara et al.*, 2014] and clearly demonstrate their interaction. On a larger scale, both continuous and discrete meter-scale rotations of stress indicators by up to 90° were observed by Shamir & Zoback [1992] in the Cajon Pass scientific borehole using borehole televiewer logs along almost 3 km. Large-scale rotations with wavelengths >100m were also observed. Distinct rotations of breakouts near fractures by 90° in an otherwise relatively homogeneous rock mass and stable tectonic setting have been observed by Rajabi et al. [2015]. Similar rotations over certain well sections were documented by Davatzes and Hickman [2006] in the 34-9RD2 well at Coso.

An absence of BOs close to fault zones that show low seismic velocities and rock density has been documented by Boness and Zoback [2004] in the SAFOD pilot hole. This can be interpreted as stress release near fault zones and in damaged rock material with reduced stiffness [*Hickman and Zoback*, 2004]. Similarly, abutting relationships between breakouts and fractures have been observed e.g. by Sahara et al. [2014] and Rajabi et al. [2015]. Sahara et al. [2014] show that rotations of BOs of up to 50° are directly related to the apparent dip direction of active natural fractures. By the way of numerical modelling, Barton & Zoback [1994] confirm that stress drops along active faults are enough to rotate the orientation of stress indicators, and explain observed rotations for a variety of tectonic and lithologic settings. They are also consistent with the modeled reduction of the local differential stress accompanying slip that correlates with the observed local absence of breakouts. Valley et al. [2014] attempt to invert the observed patterns of rotation along boreholes to infer properties of the natural

fracture network. In doing so, they follow the idea that every undulation of the local stress field can be explained by stress release on natural fractures.

Lastly, frequent changes of lithology (Figure 10e) can be associated with varying stress fields and fracture patterns [*Bai et al.*, 2002; *Bourne*, 2003]. Rock units of greater stiffness tend to concentrate stresses. As seen in the deepest part of well 58A-10^v, the stiffer but less strong diorite section shows a different failure pattern accompanied by considerable rotation of the local stress field. However, since the horizontal principal stresses at Coso have greatly different magnitudes, it is unlikely that the amplitude of local stress rotations can be explained solely by heterogeneity of elastic parameters of single rock units. For heterogeneous distribution of elastic parameters as deduced from velocity logs in the KTB well, for example, rotations of the orientation of S_{Hmax} are expected to be less than about 5° [*Langenbruch and Shapiro*, 2014].

In accordance with previous work on vertical wells, we assumed that the vertical stress is a principal stress component and all local rotations occur between the horizontal principal stress components. It may be more physically realistic to expect the stress tensor to rotate freely about all three axes, and the magnitudes of the principal stresses to vary. Therefore, the observed local stress rotations modelled as rotations about the vertical axis are an incomplete proxy for the true rotation of the stress tensor. Given that the propagation of induced fractures is highly perturbed by the presence of natural fractures and mechanical heterogeneities in the rock, we consider it impossible to resolve the true local rotation of the stress tensor in 3-D unless exceptional conditions related to the well trajectory and homogeneity of the formation are met.

5.2 Dependence on sampling interval length

The analyzed boreholes are not only closely spaced, but the two logs span about 2 km of each well trajectory. More typically, image logs are acquired only in target horizons – sections only a few hundred meters thick at best. It is obvious that we would obtain a biased view of the stress field along the borehole trajectories if only short sections were logged. To quantify such bias, we mask the image logs with random windows of given length and estimate the mean stress orientation and SD as if only data from these intervals were available. For each interval length, we randomly place 1000 windows over the interpreted logs. The range of values for the mean stress orientation and SD obtained for each interval length is presented using box plots in Figure 11. Horizontal lines represent the respective value obtained for the entire log, termed "true" values here for simplicity.

We first discuss the mean stress orientation (Figure 11a-b). For the vertical well and intervals lengths <400 m, the central two quartiles spread within 10° of the true value. Outliers may be much further away from the true value. These extreme outliers and the range of the central quartiles are significantly reduced at intervals lengths of ≥400 m. For the same windows, SD (Figure 11c-d) increases significantly from a median of 13° for an interval length of 50 m to 23° for an interval length of 600 m and longer. As expected, the spread of obtained values of SD reduced with longer interval length. Critically, short log intervals tend to yield a smaller SD although the obtained mean stress orientation has a significant deviation from the true mean stress orientation. Therefore, the standard deviation has limited value for quantifying the quality of a stress measurement and it needs to be complemented by the length of the interval over which stress indicators were observed. The deviated well (Figure 11c-d) shows a very similar behavior with an even larger scatter of the mean stress orientation about the true value for short

log intervals. Similarly, the obtained SD converges to the true value only for interval lengths of at least 600 m.

In Figure 11e-f we show the distribution of quality rankings that would be obtained for the windows based on the WSM quality ranking [*Heidbach et al.*, 2010]. It bases on the number of observed stress indicators, their cumulative length, and SD of observations. Given the entire range of interpreted stress indicators, the WSM quality rating is C for borehole 58A-10^v. If we evaluate separately for DIFs and BOs, we obtain quality rating B and C, respectively. For borehole 58-10^d we obtain a C quality. Contrary to WSM practice, we do not differentiate the stress measurements by type of stress indicator and treat BOs, DIFs and petal-centerline fractures equally to derive one stress measurement, SD and the corresponding quality rating. As expected, the quality ratings converge towards the rating for the entire borehole the longer the interval length is. For borehole 58A-10^v we obtain larger percentages of higher quality rating for long log intervals. However, for borehole 58-10^d and an interval length of 400 m, we obtain an almost equal mix of B and D-quality measurements, respectively with relatively few C-quality measurements in between. For longer interval lengths, the population of B-quality measurements decreases and none of these exist for interval lengths ≥ 800 m. Although larger sample lengths are more likely to be representative of the tectonic-scale processes, applying the WSM quality ranking may give them an undeserved lower weight due to their larger SD. This demonstrates the limitations of this rating scheme and demands the consideration of the interval length over which stress indicators are observed in the quality rating.
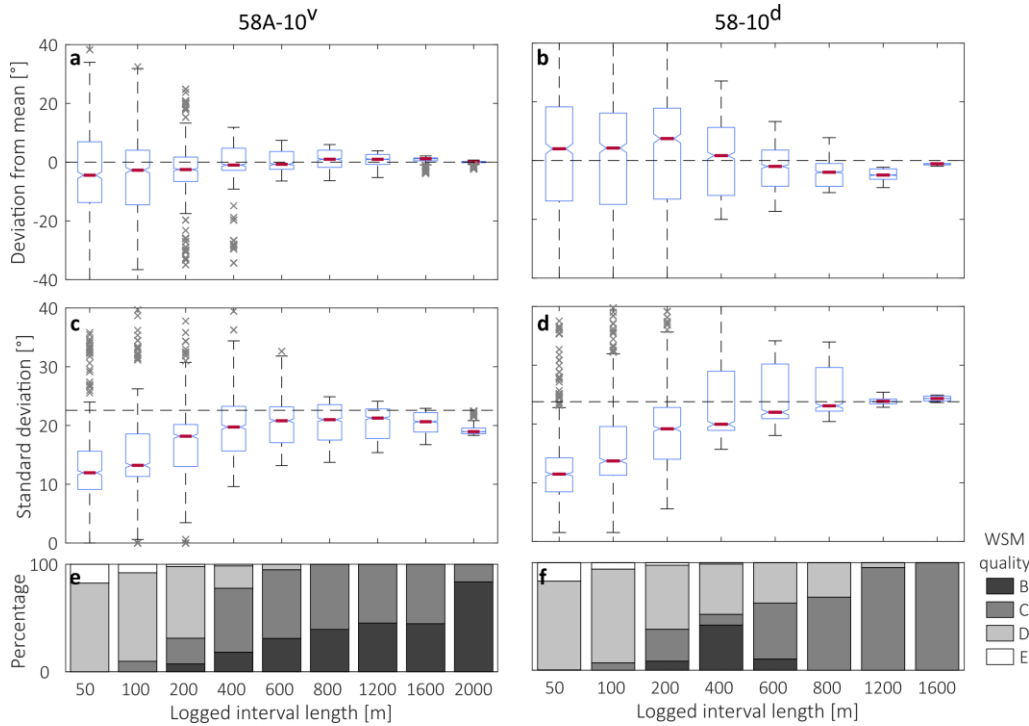

Figure 11: Variation of the obtained mean stress orientation (a and b) and SD (c and d) for randomly placed log windows of a given length. The extents of the blue rectangles represent the first and third quartiles around the median (red). Notches represent the 95% confidence interval for the median. The lower (and upper) whiskers (dashed) are the lowest (and highest) values within 1.5 times the interquartile range, i.e. the extent of the blue box. Data beyond that are marked by crosses. The dashed horizontal line represents the value obtained for the entire log without masking. The breakup of resulting WSM qualities (in percent) are shown in panels e and f.

5.3 Global data

To test whether the observed behavior of stress measurements with varying borehole log length is specific to our site or whether it is a characteristic of the stress field in the Earth's crust, we continue analyzing global data of the WSM [*Heidbach et al.*, 2010; *Heidbach et al.*, 2016]. Above, we synthetically varied the position and length of the depth interval sampled to analyze how the result is changed for a lack of data. For the WSM we can now test this on actual data that were derived under real conditions. Here the length of analyzed logs vary from 1 m to more than 6 km.

We use the latest 2016 release of the WSM that contains more than 42,000 data records. The WSM contains data from a multitude of stress measurement techniques and here we restrict our analysis to stress measurements derived from borehole breakouts and drilling-induced fractures. In the WSM borehole breakout data are subdivided into types BO for analysis of individual breakouts, BOC for analysis of the cross-sectional shape of the entire well, and BOT for televiewer-imaged shapes of individual breakouts. We do not follow this subdivision and lump all DIF and BO data together. The log length is calculated from the difference between the top and bottom true vertical depth of stress indicators. As the vast majority of measurements are from vertical wells, we use this interval as the log length. Wells with a reported SD of zero and E-quality measurements (SD > 40°) are discarded. In total, we retain 3,986 measurements with a complete data set.

Again, we use box plots to analyze the distribution of reported standard deviations for bins of the logged interval (Figure 12). We observe a clear increase of SD with interval length for intervals < 900 m. The median value of SD increases from 7° for intervals < 100 m to 15° for intervals > 1000 m. For intervals longer than that, the median of observed SD is approximately constant at 15°. This is the same behavior we have observed before in boreholes 58-10^d and 58A-10^v: an increase of the observed SD before it reached a stable level. In the case of the Coso wells however, this stable level is higher than for the median of global well data. We hypothesize that the higher level of stress heterogeneity is related to the structural complexity of the subsurface in the Coso Wash region with frequent lithology changes (Figure 8) and a dense fracture network as revealed from image logs. The latter is a result of the strong deformation of the area, which is part of the Eastern California Shear Zone that accommodates about one quarter of the relative plate motion between the Pacific and the North American plates [*Unruh et al.*, 2002]. Consequently, the Coso area is among the most seismically active areas in California [*Schoenball et al.*, 2015].

The constant value for the median SD reported for horizontal principal stress determinations on logs of more than 900 m indicates that SD is indeed a site characteristic and an appropriately long borehole log is required to resolve this characteristic. It appears that below log lengths of about 1 km analyses are biased toward relatively low values of SD.
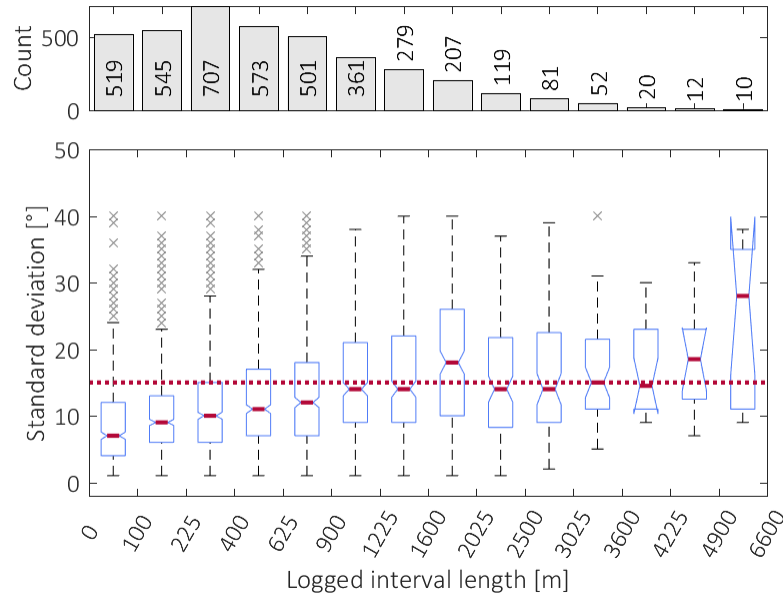
Figure 12: Boxplots of SD as a function of the logged interval for global World Stress Map data derived from BOs and DIFs, A-D qualities. Upper panel shows the number of data records in each bin of interval length. The red line represents the median SD for intervals ≥ 1000 m. See Figure 11 for explanation of the box plots.

6 Conclusions

We have analyzed stress indicators in a pair of wells adjacent to the Coso Geothermal Field. Both wells have a large number of stress indicators along their logged intervals. Despite the strong deviation of 58-10[d], both logged well trajectories sample a much larger vertical extent (≈ 2 km) than the lateral separation of the well trajectories (<0.3 km). It is thus reasonable to expect that both wells sample similar stress fields and both are subjected to similar changes in the stress field at greater depth. And indeed, we find the same mean stress orientation with S_{Hmax} oriented at N23°E and the same standard deviation of stress indicators of 23° in both wells.

Including deviated sections of boreholes in stress analysis is principally more informative than analyzing only sub-vertical sections, since the stress tensor is sampled in various directions. Depending on borehole trajectory, stress indicators identified in deviated wells can inform the stress regime, unlike those in sub-vertical boreholes.

We test the bias in our results for cases where only shorter intervals of image logs are available. For both boreholes we observe an increase of SD with increasing logged interval, for lengths <600 m. With longer interval length, the obtained stress orientations and standard deviations converge towards the same values for both boreholes. We therefore conclude that the tectonic stress field given by the orientation of the tectonic stress tensor and the heterogeneity at the location of the 58-10 well pad is well characterized. The scatter of observed stress indicators quantified by SD appears to be an intrinsic property of the stress field in the highly fractured crystalline rock of the site.

We checked for the same bias in borehole failure-derived stress measurements of the WSM. A trend towards larger SD for longer interval length was found, with SD converging for lengths >1 km. This demonstrates that (1) stress heterogeneity quantified using SD is a site characteristic and (2) that stress

measurements over intervals >1 km are necessary to reliably characterize that heterogeneity by SD values. Based on these findings, we suggest alternative criteria to assess the quality of stress measurements. Besides the number and cumulative length of stress indicators and their standard deviation, other critical parameters for the quality of stress measurements to be considered are the length of the interval that is sampled using stress indicators and whether or not there is a stress rotation with depth.

Similar as Bailey et al. [2010] do for fault zones, we find evidence for a characteristic length scale and hence a breakdown of self-similarity of the stress field around boreholes. This is consistent with the previous studies by Shamir and Zoback [1992] and Day-Lewis et al. [2010] who could establish self-similar behavior on shorter wavelengths, but did not have sufficient data for characteristic lengths beyond about 100 m. This is also consistent with regional studies, that show coherent domains of stress over 100s of km [*Müller et al.*, 1992; *Zoback*, 1992; *Heidbach et al.*, 2010, *Reiter et al.*, 2014]. If the stress field was self-similar at all scales, we would expect SD to steadily increase with longer log length. Further analysis of stress heterogeneity around the 1 km length scale could help to resolve the dispute between scale-free self-similarity of stress heterogeneity [*Smith and Heaton*, 2011] and a smooth stress field [*Hardebeck*, 2010]. Better understanding of the reservoir-scale stress heterogeneity has major implications for engineering applications, such as probabilistic hazard estimation of faults with known orientation. Furthermore, the pattern of the stress heterogeneity on faults is a major ingredient of our understanding of the dynamics of rupture with known links to the magnitude-frequency relation.

Acknowledgements

References

Aadnoy, B. S. (1990a), Inversion technique to determine the in-situ stress field from fracturing data, *J. Pet. Sci. Eng.*, *4*(2), 127–141.

Aadnoy, B. S. (1990b), In-situ stress directions from borehole fracture traces, J. Pet. Sci. Eng., 4(2), 143–153, doi:10.1016/0920-4105(90)90022-U.

Ampuero, J., J. Ripperger, and P. M. Mai (2006), *Earthquakes: Radiated Energy and the Physics of Faulting*, Geophysical Monograph Series, edited by R. Abercrombie, A. McGarr, H. Kanamori, and G. Di Toro, American Geophysical Union, Washington, D. C.

Anderson, E. M. (1951), *The dynamics of faulting and dyke formation with applications to Britain*, Oliver and Boyd, Edinburgh, UK.

Andrews, D. J. (1980), A stochastic fault model: 1. Static case, *J. Geophys. Res. Solid Earth*, *85*(B7), 3867–3877, doi:10.1029/JB085iB07p03867.

Bai, T., L. Maerten, M. R. Gross, and A. Aydin (2002), Orthogonal cross joints: do they imply a regional stress rotation?, *J. Struct. Geol.*, *24*(1), 77–88, doi:10.1016/S0191-8141(01)00050-5.

Bailey, I. W., Y. Ben-Zion, T. W. Becker, and M. Holschneider (2010), Quantifying focal mechanism heterogeneity for fault zones in central and southern California, *Geophys. J. Int.*, *183*(1), 433–450, doi:10.1111/j.1365-246X.2010.04745.x.

Barton, C. A., and D. Moos (2010), Geomechanical wellbore imaging: Key to managing the asset life cycle, in *Dipmeter and borehole image log technology: AAPG Memoir 92*, edited by M. Poppelreiter, C. Garcia-Carballido, and M. Kraaijveld, pp. 81–112, doi: 10.1306/13181279M922689.

Barton, C. A., and M. D. Zoback (1992), Self-similar distribution and properties of macroscopic fractures at depth in crystalline rock in the Cajon Pass Scientific Drill Hole, *J. Geophys. Res.*, *97*(B4), 5181, doi:10.1029/91JB01674.

Barton, C. A., and M. D. Zoback (1994), Stress perturbations associated with active faults penetrated by boreholes: Possible evidence for near-complete stress drop and a new technique for stress magnitude measurement, *J. Geophys. Res.*, *99*(B5), 9373, doi:10.1029/93JB03359.

Bell, J. S., and D. I. Gough (1979), Northeast-southwest compressive stress in Alberta evidence from oil wells, *Earth Planet. Sci. Lett.*, *45*(2), 475–482, doi:10.1016/0012-821X(79)90146-8.

Bell J.S., G. Caillet, and J. Adams (1992), Attempts to detect open fractures and non-sealing faults with dipmeter logs, *Geol Soc London, Spec Publ*. 1992;65(1):211-220, doi:10.1144/GSL.SP.1992.065.01.16.

Ben-Zion, Y. (2008), Collective behavior of earthquakes and faults: Continuum-discrete transitions, progressive evolutionary changes, and different dynamic regimes, *Rev. Geophys.*, *46*(4), doi:10.1029/2008RG000260.

Blankenship, D. et al. (2016), Frontier Observatory for Research in Geothermal Energy: Phase 1 Topical Report West Flank of Coso, CA, Sandia Report, SAND2016-8930.

Bobet, A., and H. H. Einstein (1998), Fracture coalescence in rock-type materials under uniaxial and biaxial compression, *Int. J. Rock Mech. Min. Sci.*, *35*(7), 863–888, doi:10.1016/S0148-9062(98)00005-9.

Boness, N. L., and M. D. Zoback (2004), Stress-induced seismic velocity anisotropy and physical properties in the SAFOD Pilot Hole in Parkfield, CA, *Geophys. Res. Lett.*, *31*(15), L15S17, doi:10.1029/2003GL019020.

Bourne, S. J. (2003), Contrast of elastic properties between rock layers as a mechanism for the initiation and orientation of tensile failure under uniform remote compression, *J. Geophys. Res.*, *108*(B8), 2395, doi:10.1029/2001JB001725.

Candela, T., F. Renard, Y. Klinger, K. Mair, J. Schmittbuhl, and E. E. Brodsky (2012), Roughness of fault surfaces over nine decades of length scales, *J. Geophys. Res. Solid Earth*, *117*(B8), B08409, doi:10.1029/2011JB009041.

Cornet, F. H., T. Bérard, and S. Bourouis (2007), How close to failure is a granite rock mass at a 5 km depth, *Int. J. Rock Mech. Min. Sci.*, *44*(1), 47–66, doi:10.1016/j.ijrmms.2006.04.008.

Davatzes, N. C., and S. H. Hickman (2006), Stress and faulting in the Coso geothermal field: Update and recent results from the East Flank and Coso Wash, in *Stanford Geothermal Workshop, Proceedings, 31st Workshop on Geothermal Reservoir Engineering,* p. 12, Stanford Univ., Stanford, Calif.

Davatzes, N. C., and S. H. Hickman (2010), The Feedback Between Stress, Faulting, and Fluid Flow: Lessons from the Coso Geothermal Field, CA, USA, in *World Geothermal Congress*, pp. 25–29, Bali, Indonesia.

Davatzes, N. C., and S. H. Hickman (2010), Stress, Fracture, and Fluid-flow Analysis Using Acoustic and Electrical Image Logs in Hot Fractured Granites of the Coso Geothermal Field, California, U.S.A., in *Dipmeter and borehole image log technology: AAPG Memoir 92*, edited by M. Poppelreiter, C. Garcia-Carballido, and M. Kraaijveld, pp. 259–293, doi:10.1306/13181288M923134.

Day-Lewis, A., M. D. Zoback, and S. H. Hickman (2010), Scale-invariant stress orientations and seismicity rates near the San Andreas Fault, *Geophys. Res. Lett.*, *37*, L24304, doi:10.1029/2010GL045025.

Eckert, A., and P. Connolly (2007), Stress and fluid-flow interaction for the Coso Geothermal Field derived from 3D numerical models, *GRC Trans.*, *31*, 385-390.

Feng, Q., and J. M. Lees (1998), Microseismicity, stress, and fracture in the Coso geothermal field, California, *Tectonophysics*, *289*(1-3), 221–238, doi:10.1016/S0040-1951(97)00317-X.

GMI (2003), Fracture permeability and in situ stress in the eastern extension of the Coso Geothermal Field, *Geomechanics International, Inc.*, Final Report.

Hardebeck, J. (2010), Aftershocks are well aligned with the background stress field, contradicting the hypothesis of highly heterogeneous crustal stress, *J. Geophys. Res. Solid Earth*, *115*(12), B12308, doi:10.1029/2010JB007586.

Hardebeck, J. L. (2006), Homogeneity of small-scale earthquake faulting, stress, and fault strength, *Bull. Seismol. Soc. Am.*, *96*(5), 1675–1688, doi:10.1785/0120050257.

Hardebeck, J. L. (2015), Comment on "Models of Stochastic, Spatially Varying Stress in the Crust Compatible with Focal Mechanism Data, and How Stress Inversions Can Be Biased toward the Stress Rate" by Deborah Elaine Smith and Thomas H. Heaton, *Bull. Seismol. Soc. Am.*, *105*(1), 447–451, doi:10.1785/0120130127.

Hauksson, E., W. Yang, and P. M. Shearer (2012), Waveform relocated earthquake catalog for southern California (1981 to June 2011), *Bull. Seismol. Soc. Am.*, *102*(5), 2239–2244, doi:10.1785/0120120010.

Healy, D., R. R. Jones, and R. E. Holdsworth (2006), Three-dimensional brittle shear fracturing by tensile crack interaction, *Nature*, *439*(7072), 64–67, doi:10.1038/nature04346.

Heidbach, O., M. Rajabi, K. Reiter, M. Ziegler, and WSM Team (2016), World Stress Map Database Release 2016, *GFZ Data Services*, doi:10.5880/WSM.2016.001.

Heidbach, O., J. Reinecker, M. Tingay, B. Müller, B. Sperner, K. Fuchs, and F. Wenzel (2007), Plate boundary forces are not enough: Second- and third-order stress patterns highlighted in the World Stress Map database, *Tectonics*, *26*(6), doi:10.1029/2007TC002133.

Heidbach, O., M. Tingay, A. Barth, J. Reinecker, D. Kurfeß, and B. I. R. Müller (2010), Global crustal stress pattern based on the World Stress Map database release 2008, *Tectonophysics*, *482*(1-4), 3–15, doi:10.1016/j.tecto.2009.07.023.

Hickman, S. H., and M. D. Zoback (2004), Stress orientations and magnitudes in the SAFOD pilot hole, *Geophys. Res. Lett.*, *31*(15), L15S12, doi:10.1029/2004GL020043.

Hiramatsu, Y., and Y. Oka (1962), Stress around a shaft or level excavated in ground with a three-dimensional stress state. Mem. Fac. Engng. Kyoto Univ. 24, 56–76.

Hsu, Y.-J., L. Rivera, Y.-M. Wu, C.-H. Chang, and H. Kanamori (2010), Spatial heterogeneity of tectonic stress and friction in the crust: new evidence from earthquake focal mechanisms in Taiwan, *Geophys. J. Int.*, *182*(1), 329–342, doi:10.1111/j.1365-246X.2010.04609.x.

Huang, J., and D. L. Turcotte (1988), Fractal distributions of stress and strength and variations of b-value, *Earth Planet. Sci. Lett.*, *91*(1-2), 223–230, doi:10.1016/0012-821X(88)90164-1.

Jaeger, J. C., and N. G. W. Cook (2007), *Fundamentals of Rock Mechanics*, 2nd edn. New York, Chapman and Hall.

Jayko, A. S. (2009), Surficial Geology of the Darwin Hills 30' X 60' Quadrangle, Inyo County, California, U.S. Geological Survey Scientific Investigations Map 3040, 20 p. pamphlet, 2 plates, scale 1:100,000.

Kirsch, G. (1898), Die Theorie der Elastizität und die Bedürfnisse der Festigkeitslehre, *Zeitschrift des Vereins Dtsch. Ingenieure*, *42*, 797–807.

Langenbruch, C., and S. A. Shapiro (2014), Gutenberg-Richter relation originates from Coulomb stress

fluctuations caused by elastic rock heterogeneity, *J. Geophys. Res. Solid Earth*, *119*(2), 1220–1234, doi:10.1002/2013JB010282.

Li, Y., and D. R. Schmitt (1998), Drilling-induced core fractures and in situ stress, *J. Geophys. Res. Solid Earth*, *103*(B3), 5225–5239, doi:10.1029/97JB02333.

Lockner, D. A., and N. M. Beeler (2002), Rock failure and earthquakes, in *International Handbook of Earthquake and Engineering Seismology, Part A*, pp. 505–537.

Mai, P. M., and G. C. Beroza (2002), A spatial random field model to characterize complexity in earthquake slip, J. Geophys. Res. Solid Earth, 107(B11), ESE 10-1-ESE 10-21, doi:10.1029/2001JB000588.

Mariucci M.T., A. Amato, R. Gambini, M. Giorgioni, and P. Montone (2002), Along-depth stress rotations and active faults: An example in a 5-km deep well of southern Italy, *Tectonics*, 21(4):3-9, doi:10.1029/2001TC001338.

Mastin, L. (1988), Effect of borehole deviation on breakout orientations, *J. Geophys. Res.*, *93*(B8), 9187, doi:10.1029/JB093iB08p09187.

McClusky, S. C., S. C. Bjornstad, B. H. Hager, R. W. King, B. J. Meade, M. M. Miller, F. C. Monastero, and B. J. Souter (2001), Present day kinematics of the Eastern California Shear Zone from a geodetically constrained block model, *Geophys. Res. Lett.*, *28*(17), 3369–3372, doi:10.1029/2001GL013091.

McNamara, D. D., C. Massiot, B. Lewis, and I. C. Wallis (2015), Heterogeneity of structure and stree in the Rotokawa Geothermal Field, New Zeland, *J. Geophys. Res. Solid Earth*, *120*, 1243–1262, doi:10.1002/2014JB011480.

Monastero, F. C., A. M. Katzenstein, J. S. Miller, J. R. Unruh, M. C. Adams, and K. Richards-Dinger (2005), The Coso geothermal field: A nascent metamorphic core complex, *Geol. Soc. Am. Bull.*, *117*(11), 1534, doi:10.1130/B25600.1.

Morris, A., D. A. Ferrill, and D. B. Brent Henderson (1996), Slip-tendency analysis and fault reactivation, *Geology*, *24*(3), 275, doi:10.1130/0091-7613(1996)024<0275:STAAFR>2.3.CO;2.

Morrow, C., Radney, B., Byerlee, J., 1992. Chapter 3 Frictional Strength and the Effective Pressure Law of Montmorillonite and lllite Clays, in: Evans, B., Wong, T. (Eds.), Fault Mechanics and Transport Properties of Rocks: A Festschrift in Honor of W. F. Brace. pp. 69–88. doi:10.1016/S0074-6142(08)62815-6.

Morrow, C. A., and D. A. Lockner (2006), *Physical properties of two core samples from Well 34-9RD2 at the Coso geothermal field, California*, U.S. Geological Survey, Reston, VA, United States. Open-File Report 2006-1230.

Müller, B., M. L. Zoback, K. Fuchs, L. Mastin, S. Gregersen, N. Pavoni, O. Stephansson, and C. Ljunggren (1992), Regional patterns of tectonic stress in Europe, *J. Geophys. Res.*, *97*(B8), 11783, doi:10.1029/91JB01096.

Peška, P., and M. D. Zoback (1995), Compressive and tensile failure of inclined well bores and determination of in situ stress and rock strength, *J. Geophys. Res.*, *100*(B7), 12791, doi:10.1029/95JB00319.

Pierdominici S., Mariucci M.T., and P. Montone (2011), A study to constrain the geometry of an active fault in southern Italy through borehole breakouts and downhole logs, *J Geodyn*. 2011;52(3-4):279-289, doi:10.1016/j.jog.2011.02.006.

Pierdominici S. and O. Heidbach (2012), Stress field of Italy - Mean stress orientation at different depths and wave-length of the stress pattern, *Tectonophysics*, *532-535*:301-311, doi:10.1016/j.tecto.2012.02.018.

Qian, W., and L. B. Pedersen (1991), Inversion of borehole breakout orientation data, *J. Geophys. Res.*, *96*(B12), 20093, doi:10.1029/91JB01627.

Rajabi, M., M. Tingay, R. King, and O. Heidbach (2015), Present-day stress orientation in the Clarence-Moreton Basin of New South Wales, Australia: A new high density dataset reveals local stress

rotations, *Basin Res.*, *61*, 1–19, doi:10.1111/bre.12175.

Reiter, K., O. Heidbach, D. Schmitt, K. Haug, M. Ziegler, and I. Moeck (2014), A revised crustal stress orientation database for Canada, *Tectonophysics*, 636, 111–124, doi:10.1016/j.tecto.2014.08.006.

Rivera, L., and H. Kanamori (2002), Spatial heterogeneity of tectonic stress and friction in the crust, *Geophys. Res. Lett.*, *29*(6), 12, doi:10.1029/2001GL013803.

Sahara, D. P., M. Schoenball, T. Kohl, and B. I. R. Müller (2014), Impact of fracture networks on borehole breakout heterogeneities in crystalline rock, *Int. J. Rock Mech. Min. Sci.*, *71*, 301–309, doi:10.1016/j.ijrmms.2014.07.001.

Schmitt, D. R., C. A. Currie, and L. Zhang (2012), Crustal stress determination from boreholes and rock cores: Fundamental principles, *Tectonophysics*, *580*, 1–26, doi:10.1016/j.tecto.2012.08.029.

Schoenball, M., N. C. Davatzes, and J. M. G. Glen (2015), Differentiating induced and natural seismicity using space-time-magnitude statistics applied to the Coso Geothermal field, *Geophys. Res. Lett.*, *42*(15), 6221–6228, doi:10.1002/2015GL064772.

Shamir, G., and M. D. Zoback (1992), Stress orientation profile to 3.5 km depth near the San Andreas Fault at Cajon Pass, California, *J. Geophys. Res.*, *97*(B4), 5059, doi:10.1029/91JB02959.

Sheridan, J., K. Kovac, P. E. Rose, C. A. Barton, M. J., B. Berard, J. M. Moore, S. Petty, and P. Spielman (2003), In situ stress, fracture and fluid flow analysis - East Flank of the Coso Geothermal Field, in *Stanford Geothermal Workshop*, p. 16.

Sheridan, J. M., and S. H. Hickman (2004), In situ stress, fracture, and fluid flow analysis in well 38C-9: An enhanced geothermal system in the Coso Geothermal Field, in *Stanford Geothermal Workshop*, p. 8.

Smith, D. E., and J. H. Dieterich (2010), Aftershock Sequences Modeled with 3-D Stress Heterogeneity and Rate-State Seismicity Equations: Implications for Crustal Stress Estimation, *Pure Appl. Geophys.*, *167*(8-9), 1067–1085, doi:10.1007/s00024-010-0093-1.

Smith, D. E., and T. H. Heaton (2011), Models of Stochastic, Spatially Varying Stress in the Crust Compatible with Focal-Mechanism Data, and How Stress Inversions Can Be Biased toward the Stress Rate, *Bull. Seismol. Soc. Am.*, *101*(3), 1396–1421, doi:10.1785/0120100058.

Smith, D. E., and T. H. Heaton (2015), Reply to "Comment on 'Models of Stochastic, Spatially Varying Stress in the Crust Compatible with Focal Mechanism Data, and How Stress Inversions Can Be Biased toward the Stress Rate' by Deborah Elaine Smith and Thomas H. Heaton" by Jeanne L. Hardebeck, *Bull. Seismol. Soc. Am.*, *105*(1), 452–458, doi:10.1785/0120140132.

TerraTek (2004), *Physical and mechanical properties characterization of two granitic rocks, Coso EGS Project, TerraTek Inc*, Technical Report TR04-400872, Salt Lake City, UT.

Thorsen, K. (2011), In situ stress estimation using borehole failures — Even for inclined stress tensor, *J. Pet. Sci. Eng.*, *79*(3-4), 86–100, doi:10.1016/j.petrol.2011.07.014.

Unruh, J. R., and A. R. Streig (2004), *Mapping and characterization of neotectonic structures in a releasing stepover, northern Coso Range, eastern California*, Final technical report submitted to the U.S. Navy Geothermal Program Office, China Lake Naval Air Warfare Center, Contract N68936-02-C-0208.

Unruh, J. R., E. Hauksson, F. C. Monastero, R. J. Twiss, and J. C. Lewis (2002), Seismotectonics of the Coso Range–Indian Wells Valley region, California: Transtensional deformation along the southeastern margin of the Sierran microplate, in *Geologic Evolution of the Mojave Desert and Southwestern Basin and Range: Boulder, Colorado*, edited by A. F. Glazner, J. D. Walker, and J. M. Bartley, pp. 277–294, Geological Society of America Memoir 195.

Valley, B., and K. F. Evans (2014), Preliminary assessment of the scaling relationships of in-situ stress orientation variations indicated by wellbore failure data, in *Rock Engineering and Rock Mechanics: Structures in and on Rock Masses - Proceedings of EUROCK 2014, ISRM European Regional Symposium*, pp. 463–468.

Valley, B., M. R. Jalali, M. Ziegler, and K. F. Evans (2014), Constraining DFN characteristics for deep geothermal projects by considering the effects of fractures on stress variability, in *International Discrete Fracture Network Engeneering Conference*, p. 237, Vancouver, Canada.

Wicks, C. W., W. Thatcher, F. C. Monastero, and M. A. Hasting (2001), Steady state deformation of the Coso Range, east central California, inferred from satellite radar interferometry, *J. Geophys. Res.*, *106*(B7), 13769, doi:10.1029/2001JB000298.

Wileveau, Y., F. H. Cornet, J. Desroches, and P. Blümling (2007), Complete in situ stress determination in an argillite sedimentary formation, *Phys. Chem. Earth, Parts A/B/C*, *32*(8-14), 866–878, doi:10.1016/j.pce.2006.03.018.

Wiprut, D., M. Zoback, T.-H. Hanssen, and P. Peška (1997), Constraining the full stress tensor from observations of drilling-induced tensile fractures and leak-off tests: Application to borehole stability and sand production on the Norwegian margin, *Int. J. Rock Mech. Min. Sci.*, *34*(3-4), 365.e1–365.e12, doi:10.1016/S1365-1609(97)00157-3.

Yale, D. P. (2003), Fault and stress magnitude controls on variations in the orientation of in situ stress, *Geol. Soc. London, Spec. Publ.*, *209*(1), 55–64, doi:10.1144/GSL.SP.2003.209.01.06.

Yang, W., E. Hauksson, and P. M. Shearer (2012), Computing a Large Refined Catalog of Focal Mechanisms for Southern California (1981-2010): Temporal Stability of the Style of Faulting, *Bull. Seismol. Soc. Am.*, *102*(3), 1179–1194, doi:10.1785/0120110311.

Zajac, B. J., and J. M. Stock (1997), Using borehole breakouts to constrain the complete stress tensor: Results from the Sijan Deep Drilling Project and offshore Santa Maria Basin, California, *J. Geophys. Res.*, *102*(B5), 10083, doi:10.1029/96JB03914.

Zhang, L. (2011), Three-dimensional numerical models of drilling induced core fractures, M.Sc. thesis, University of Alberta, Edmonton.

Zoback, M. D., C. A. Barton, M. Brudy, D. A. Castillo, T. Finkbeiner, B. R. Grollimund, D. B. Moos, P. Peška, C. D. Ward, and D. J. Wiprut (2003), Determination of stress orientation and magnitude in deep wells, *Int. J. Rock Mech. Min. Sci.*, *40*(7-8), 1049–1076, doi:10.1016/j.ijrmms.2003.07.001.

Zoback, M. L. (1992), First- and second-order patterns of stress in the lithosphere: The World Stress Map Project, *J. Geophys. Res.*, *97*(B8), 11703, doi:10.1029/92JB00132.

Zoback, M. D. (2010), *Reservoir Geomechanics*, Cambridge University Press.